The Astronomical Journal, 162:145 (13pp), 2021 October https://doi.org/10.3847/1538-3881/abfcbd

© 2021. The American Astronomical Society. All rights reserved.

Chemical Composition of Outbursting Comet C/2015 ER61 (PanSTARRS)

Mohammad Saki[1,9], Erika L. Gibb[1,9], Boncho P. Bonev[2,9], Nathan X. Roth[3,4,9], Michael A. DiSanti[5,6,9], Younas Khan[1,9], Neil Dello Russo[7,9], Ronald J. Vervack Jr.[7,9], Adam J. McKay[2,6,9], and Hideyo Kawakita[8,9]
[1] Department of Physics & Astronomy, University of Missouri-St. Louis, One University Blvd., St. Louis, MO, USA; msaki@mail.umsl.edu
[2] Department of Physics, American University, Washington, DC, USA
[3] Solar System Exploration Division, Astrochemistry Laboratory Code 691, NASA-Goddard Space Flight Center, Greenbelt, MD, USA
[4] Universities Space Research Association, Columbia, MD, USA
[5] Goddard Center for Astrobiology, NASA-Goddard Space Flight Center, Greenbelt, MD, USA
[6] Solar System Exploration Division, Planetary Systems Laboratory Code 693, NASA-Goddard Space Flight Center, Greenbelt, MD, USA
[7] Johns Hopkins Applied Physics Laboratory, Laurel, MD, USA
[8] Koyoma Astronomical Observatory, Kyoto Sangyo University Motoyama, Kamingamo, Kita-ku, Kyoto 603-8555, Japan

Received 2021 March 19; revised 2021 April 23; accepted 2021 April 27; published 2021 September 16

Abstract

Comet C/2015 ER61 (PanSTARRS) is a long-period Oort cloud comet whose favorable approach to the inner parts of the solar system in 2017 April–May enabled us to characterize its primary volatile composition using the iSHELL spectrograph mounted on the 3 m NASA Infrared Telescope Facility (IRTF) on Maunakea, Hawaii. We used three iSHELL settings (covering $\sim$2.8–5.2 μm) to sample fluorescent emissions from H_2O, OH, CH_3OH, HCN, C_2H_2, NH_3, CO, CH_4, C_2H_6, H_2CO, and OCS on multiple dates ranging from UT 2017 April 15 (shortly after its April 4 outburst) to May 13, nearly 30 days before the detection of its double nucleus. Our observations also offered the opportunity to obtain sensitive 3σ upper limits for cyanoacetylene (HC_3N). We report rotational temperatures ($T_{\rm rot}$), production rates (Qs), abundance (mixing) ratios (relative to H_2O and C_2H_6), and spatial distributions in the coma. ER61 exhibits variability in production rates of many species on short (day-to-day) and long (pre- versus post-perihelion) timescales. The relative abundances of these volatile species remained consistent within uncertainties during our pre-perihelion observations but tended to decrease during our post-perihelion observations (with the exception of CH_3OH and HCN). The short-timescale variability in the production rates of these volatiles could be due to diurnal effects (over the course of the rotation of the nucleus) and/or the effect of its outburst. The decrease in the production rates and hence the mixing ratios in some volatiles in post-perihelion dates could be due to the presence of seasonal effects in ER61.

Unified Astronomy Thesaurus concepts: Long period comets (933); Near infrared astronomy (1093); Comet volatiles (2162); High resolution spectroscopy (2096)

1. Introduction

Comets are small, volatile-rich, relatively unprocessed remnants of the early solar system. They formed in the protosolar nebula in the giant planet region between 5 and 30 AU (or more) from the Sun. They were ejected into their current stable dynamical reservoir of either the Oort cloud (Vokrouhlický et al. 2019) or the Kuiper Belt (Nesvorný et al. 2017) by the migration of giant planets. Owing to their small size, comets lack a known mechanism for internal self-heating; thus, it is likely that the interior compositions of comets have not been significantly modified and should reflect the composition and the conditions where (and when) they formed (Bockelée-Morvan et al. 2004; Mumma & Charnley 2011). Owing to increasing solar radiation as comets enter the inner solar system (heliocentric distance <3 AU), a freely expanding atmosphere (i.e., coma) along with a dust tail and ion tail will form. We can study these features using spectroscopy. The primary volatile composition of the coma can be used as a proxy for the chemical composition of its nucleus and therefore provide insights into the initial conditions and subsequent evolution of the early solar system.

Long-period Oort cloud comets (OCCs; which originate from the Oort cloud and have long orbital periods) represent excellent targets for study as their nuclei have likely been less modified since their formation than those of short-period comets (Vokrouhlický et al. 2019). Most processes that can change the properties of comet nuclei only affect a thin layer (a few meters deep) from the surface, which is thought to be excavated over the course of a perihelion passage into the inner solar system (Stern 2003; Le Roy et al. 2015; Saki et al. 2020a; Gronoff et al. 2020). This emphasizes the importance of obtaining both pre- and post-perihelion observations of comets whenever possible. Some comets exhibit a sudden eruption of materials, referred to as an outburst, close to their perihelion passage. Outbursts are known to start with the sudden appearance and steep brightening of an unresolved plume of material and are often described by a nuclear magnitude (Sekanina 2010, 2017). Comets that outburst represent additional opportunities to probe the likely more pristine material below a comet's topmost surface layers.

High-resolution infrared (IR) spectroscopy is a valuable way to characterize the primary volatile composition of the nucleus through analysis of fluorescent emissions in the coma. Coupled with protoplanetary disk models, the nucleus composition inferred from these studies may place observational constraints on the physics and chemistry operating in the nascent protoplanetary disk midplane where comets formed. With about 40 comets characterized in the IR and radio and more than 200 comets cataloged in photodissociation products at optical wavelengths, a large number of species have been identified in cometary atmospheres, both from ground- and space-based observations

---

[9] Visiting Astronomer at the Infrared Telescope Facility, which is operated by the University of Hawai'i under contract NNH14CK55B with the National Aeronautics and Space Administration.

(e.g., Biver et al. 2015; Cochran et al. 2015; Le Roy et al. 2015; Dello Russo et al. 2016b; Roth et al. 2018; Saki et al. 2020a, 2020b).

Certain primary volatiles—C_2H_2, CO, CH_4, and OCS—are under-represented in studies of comets as a whole (Dello Russo et al. 2016a; Saki et al. 2020a). IR coma studies indicate that Jupiter-family comets (JFCs; which originate from the Kuiper Belt and have short orbital periods) are in general depleted relative to OCCs in the hypervolatiles CO and CH_4, which may reflect the effects of repeated close perihelion passages on their volatile content (Dello Russo et al. 2016a; Saki et al. 2020b; Roth et al. 2020). On the other hand, large optical surveys of product species found no correlation between the depleted chemistry and dynamical age in JFCs, suggesting that compositional differences may instead be primordial and indicative of differences in formation histories for JFCs compared to OCCs (A'Hearn et al. 1995). The detection of crystalline silicates in some comets, coupled with updates in dynamical models (e.g., Levison et al. 2011), suggests that scattering processes and large-scale mixing of materials in the early solar nebula have complicated the distinction between comet-forming regions (Bockelée-Morvan et al. 2000; Gomes et al. 2005; Zolensky et al. 2006; Dello Russo et al. 2016b; Bockelée-Morvan et al. 2016). Therefore, both the Oort cloud and Kuiper Belt could contain comets that represent varying (or, at the other extreme, largely overlapping) formation regions in the solar nebula. The Rosetta mission to comet 67P/Churyumov–Gerasimenko (hereafter 67P) revealed a heterogeneous nucleus, adding more complexity to these scenarios (Le Roy et al. 2015; Rickman et al. 2015; A'Hearn 2017).

C/2015 ER61 (PanSTARRS; hereafter ER61) was a long-period OCC that was observed in multiple wavelength regimes. In the radio, Roth et al. (2021) reported production rates of HCN, CS, CH_3OH, H_2CO, and HNC along with an upper limit for CO using the Atacama Large Millimeter/Submillimeter Array (ALMA) on April 11 and 15. Opitom et al. (2019) reported results from optical observations of ER61 using the Multi-Unit Spectroscopic Explorer (MUSE) and produced simultaneous maps of CN, C_2 and NH_2 and dust particles on April 9, showing their release mechanism and also extended dust emissions. Yang et al. (2018) obtained high-resolution spectra of ER61 with the Ultraviolet and Visual Echelle Spectrograph at Very Large Telescope (UVES/VLT) on UT 2017 April 13 and 17 and reported carbon and nitrogen isotopic ratios.

In this work we characterize the primary chemical composition of ER61 from near-IR ($\lambda \sim 2.8$–$5.2\,\mu$m) spectroscopy shortly after its UT 2017 April 4 outburst. We report the detection of H_2O, OCS, C_2H_6, CH_3OH, H_2CO, NH_3, C_2H_2, and HCN, as well as stringent 3σ upper limits for CO, CH_4, and HC_3N. In Section 2, we discuss the outburst of ER61. In Section 3, we discuss our observations and our data reduction methodology. In Section 4, we present our results. In Section 5, we discuss our results and place them in the context of comets characterized to date.

2. Outburst In ER61

Outbursts appear to be activated by gases released from a reservoir of a highly volatile material stored in the nucleus that heats up and/or becomes pressurized as the comet gets closer to the Sun (Sekanina 2017). An in situ example is provided by cliff collapses in comet 67P's northern and southern hemispheres and outbursts near the sharp boundary in the small lobe observed in 2015, during the Rosetta mission (Vincent et al. 2016; El-Maarry et al. 2017; Pajola et al. 2017). The products observed during an outburst are the escaping gases and ice/dust grains that are dragged from the nucleus by the released gases, and outbursts are characterized as gas dominated or dust dominated depending on which component prevails (see Sekanina 2017 for details).

These two types of outbursts (dust or gas dominated) have both similarities and differences (see Figure 6 in Sekanina 2017). An important similarity is an active phase: the activity of the outburst source on the nucleus begins at the time of onset and terminates at the time of peak magnitude. The duration of the active phase is thus defined as the interval between the onset and the peak. The light curves can be used to distinguish between the two types of outbursts. Dust-dominated outbursts are exemplified by a plateau during which the comet's brightness subsides gradually. Gas-dominated outbursts are characterized by a steep decline in brightness after the peak that nearly mirrors the initial brightening (see Section 2.4 of Sekanina 2017 for details). This occurs because the brightness variations in the gas-dominated outbursts are determined by the fairly short dissociation and ionization lifetimes of the radiating molecules in the coma, coupled with relatively high gas velocities ($\sim$1 km s^{-1}). Because of the lower velocities of solid particles, however, the residence times of dust in the coma are substantially longer than those of radiating molecules, so a post-peak plateau in the dust-dominated outbursts is observed.

If the outburst is preceded by one or more precursor eruptions, the event becomes a composite explosion. Dust particles might also fragment in the coma, expanding their total cross-sectional area and increasing the comet's brightness over a longer period of time; such a scenario is referred to as an extended dust-dominated outburst (Sekanina 2010, 2017). The sources of outbursts typically have a fairly limited extent on the scale of nuclear dimensions, so most outbursts can be classified as either local or regional episodes. Under exceptional conditions, a major part of the nucleus may be involved. Such events are global in extent, with potentially severe implications for the comet's future evolution; they are referred to as giant explosions (Sekanina 2010, 2017). However, most cometary outbursts appear to be fairly short-lived, at least in terms of the total brightness, with the light curve exhibiting a sharp peak rather than a plateau, and thus no signature of dust dominance (see Figures 1–4 in Sekanina 2017; Clements & Fernandez 2021).

Outbursts have been observed in many comets such as 29P/Schwassmann-Wachmann 1 (Wierzchos & Womack 2020), 73P/Schwassmann-Wachmann (Kobayashi et al. 2007), 168P/Hergenrother (Sekanina 2014), 17P/Holmes (Shinnaka et al. 2018), and 1P/Halley (Gronkowski 2002), and in the extreme signifying disruption of the nucleus in comets such as C/2001 A2 (Sekanina et al. 2002) and C/1999 S4 (Chubko et al. 2005; Dello Russo et al. 2005). Examination of the visual light curve for ER61 indicates that its magnitude was 8.3 on UT April 3.8 (equal in brightness to two days earlier), whereas 9 hr later, on UT April 4.17, it was estimated to be 7.4, 0.7 magnitude brighter, implying a brightening rate of 1.9 mag per day. This suggests that the outburst likely started on UT April 3.9 ± 0.1 and peaked on UT April 6.5 (±1 day). The overall variation in amplitude amounted to 2.1 ± 0.1 mag (see Section 4 of Sekanina 2017 for a detailed discussion).

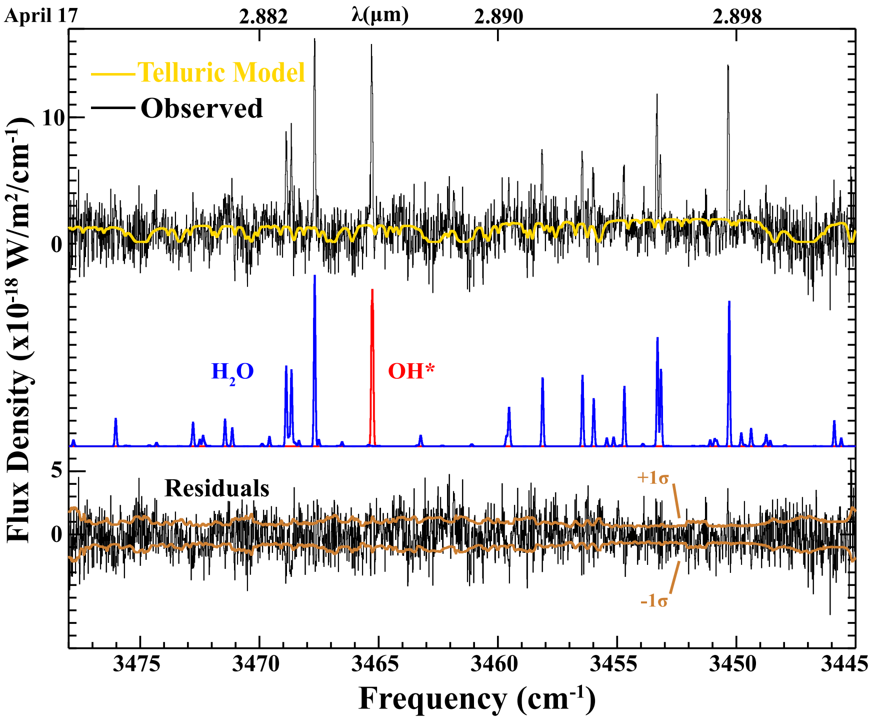

Figure 1. Extracted spectra showing fluorescence emission of H_2O and OH^* in ER61, superimposed on the cometary continuum on UT 2017 April 17. The yellow trace overplotted on the uppermost cometary spectrum is the best-fit telluric transmittance model (convolved to the instrumental resolution). The fluorescence emission models of H_2O and OH^* (color-coded for clarity) are plotted below. At the bottom of the panel is the residual spectrum (after subtracting the telluric absorption model and the fluorescence models), with the 1σ uncertainty envelope overplotted in bronze.

Two months after its outburst, on UT 2017 June 13, a double nucleus was observed, a faint companion, of apparent magnitude $\sim$16, located in the primary's coma but displaced $\sim 0\farcm2$ in the anti-sunward direction (Sekanina 2017). An in-depth investigation of the companion's motion and its variable magnitude over a course of three weeks in 2017 June–July was conducted by Sekanina (2017). Given the temporal correlations between outbursts and nucleus fragmentation of many comets, Sekanina (2017) concluded that the observed outburst and nuclear fragmentation of ER61 might be the products of the same event (Sekanina 2017). Our ER61 April observations were conducted approximately 11 days after its major outburst, and our May observations were conducted about 30 days before the first detection of its double nucleus.

3. Observations and Data Reduction

ER61 is a long-period OCC, which was first spotted in several images taken under the auspices of the Pan-STARRS project with the 180 cm f/2.7 Ritchey–Chretien reflector on Haleakala, Maui, on 2015 March 14–15 (Tubbiolo et al. 2015; Sekanina 2017). It was originally classified as an asteroid (2015 ER61) by the Minor Planet Center (2015), even though it was almost 9 AU from the Sun and following a nearly parabolic orbit (Sekanina 2017). The object was subsequently detected in several earlier Pan-STARRS images from 2015 January and February (Tubbiolo et al. 2015). When signs of cometary activity were first noticed in late December 2015 and confirmed in 2016 January, the object was reclassified as a long-period comet (Sekanina 2017).

ER61 reached perihelion (1.042 AU) on UT 2017 May 9.77, approximately 35 days after its major outburst on April 4, and was closest to Earth (1.18 AU) on UT 2017 April 18. We observed ER61 on UT 2017 April 15–17 (near closest approach to Earth) and May 11–13 (near perihelion) using the high-resolution ($\lambda/\Delta\lambda$ $\sim$40,000) IR immersion grating echelle spectrograph iSHELL (Rayner et al. 2012, 2016) at the 3 m NASA Infrared Telescope Facility (IRTF) on Maunakea, HI. We characterized ER61 using three iSHELL settings: (1) our custom *L*-band setting ("Lcustom", $\sim$2.8–3.1 μm) that contains emissions from C_2 H_2, HCN, NH_3, and H_2O; (2) the M2 setting ($\sim$4.5–5.2 μm) that samples emissions of OCS, CO, and H_2O; and (3) the Lp1 setting ($\sim$3.2–3.6 μm) that samples emission lines of CH_4, C_2H_6, CH_3OH, H_2CO, and OH^* (OH^* represents OH from prompt emission, which is a direct proxy for the production and spatial distribution of H_2O; see Bonev et al. 2006). The fluorescence emissions of H_2O in the Lcustom setting sample a range of excitation energies and enable a robust determination of rotational temperature (see Figure 1 and Section 4.3). We also determined rotational temperatures for C_2H_6, HCN, and CH_3OH, which were all found to be consistent with that for H_2O, although less well constrained.

Table 1 shows our observing log for comet ER61. Observations were performed with a $0\farcs75$ (six-pixel) wide slit, oriented along the projected Sun–comet line with position angle (PA) $\sim$252° on all dates. All observations were performed using a standard ABBA nod pattern (sequence of four scans) where the A and B beams were placed symmetrically about the midpoint along the 15″ long slit and separated by half its length. Thus, the comet was present in both beams, thereby providing increased signal to noise (by a factor of up to $\sqrt{2}$ compared with nodding to blank sky).

Combining the frames as A-B-B+A (comet-sky-sky+comet) canceled out background thermal continuum, sky emission (lines and continuum), and instrumental biases to second order in airmass (see Figure 2 of DiSanti et al. 2001). The data were cleaned of cosmic ray hits and hot pixels and

Table 1
Observing Log for ER61

UT Date (2017)	iSHELL Setting	UT time	R_h (AU)	Δ (AU)	$d\Delta/dt$ (km s^{-1})	T_{int} (minutes)	Slit PA
April 15	Lp1	15:29–15:48	1.11	1.18	−2.29	20	253°
April 16	Lp1	15:24–17:44	1.11	1.17	−1.62	76	252°
	Lcustom	18:37–20:12	1.11	1.17	−1.25	44	252°
April 17	Lcustom	15:01–15:40	1.10	1.17	−1.19	36	252°
May 11	Lp1	14:29–15:44	1.04	1.24	8.94	96	250°
May 12	M2	14:16–17:16	1.04	1.25	9.21	94	250°
	Lp1	17:36–19:25	1.04	1.25	9.56	60	250°
May 13	Lcustom	14:34–20:55	1.04	1.25	9.68	80	250°

Note. R_h, Δ, and $d\Delta/dt$ are the heliocentric distance, geocentric distance, and geocentric velocity, respectively, of ER61, and T_{int} is total integration time on source. The slit position angle (PA) was oriented along the projected Sun–comet line on all dates.

rectified to produce two-dimensional (spatial-spectral) frames, where each row corresponds to a constant (and unique) spatial position along the slit and each column to a unique wavelength.

The Planetary Spectrum Generator (Villanueva et al. 2018), optimized for Maunakea's atmospheric conditions, was used to generate atmospheric models, to assign wavelength scales to the spectra, and to establish absolute column burdens of the component absorbing species in the terrestrial atmosphere. The atmospheric models were binned to the resolution of the comet spectrum and scaled to the comet's continuum intensity. They were then subtracted from each row of the cometary spectra; co-addition of multiple rows (15 rows, approximately 2.″5) resulted in the comet emission spectra. Figure 1 shows this procedure. The fully resolved best-fit model provided a precise value for the transmittance at each Doppler-shifted line position. Our observational procedures and data reduction algorithms have been rigorously tested and well documented in peer-reviewed literature (Dello Russo et al. 1998; DiSanti et al. 2001; Bonev 2005; DiSanti et al. 2006; Villanueva et al. 2009; Radeva et al. 2010; DiSanti et al. 2014, 2017). We note that spatially resampling using a third-order polynomial more completely removed the curvature in the spatial dimension from iSHELL frames, so we employed this in place of the previously used second-order polynomials (DiSanti et al. 2017; Roth et al. 2018).

For flux calibration, a suitably bright IR flux standard star was observed using a 4″ wide slit on each date and for each setting (using a wider slit for the star than was used for the comet helps minimize loss of signal and thereby achieve a truer measure of the stellar continuum; see Bonev 2005; Radeva et al. 2010; Villanueva et al. 2011a, 2011b for further details regarding flux calibrations). Seeing was consistently ~0.″7 in our April dates. It was ~0.″6 on UT May 11, and ~0.″8 and 0.″7 on UT May 12 and May 13, respectively.

4. Results

We determined rotational temperatures ($T_{\rm rot}$), volatile production rates (Q, molecules s^{-1}), and the abundance (or "mixing") ratios $Q_X/Q_{\rm H2O}$ (expressed in percent) for volatile species in ER61. We found consistent results and excellent fits to the comet spectra, both for telluric absorptions and for cometary emission features.

4.1. Spatial Profiles

Long-slit high-resolution IR observations of comets permit investigations of processes in the inner coma, where both nucleus and extended sources (i.e., release from one or more sources in the coma) may contribute to the production and spatial distribution of a particular volatile. Analysis of spatial profiles of emissions for coma molecules can indicate whether their distributions differ from that expected for direct sublimation from the nucleus, as opposed to release from extended sources in the coma (Dello Russo et al. 1998; DiSanti et al. 2001; Brooke et al. 2003; Dello Russo et al. 2016a). The spatial profiles for molecules produced by direct sublimation peak in intensity at (or at least near) the position of the nucleus before falling off with increasing nucleocentric distance (ρ) as ρ^{-1} whereas molecules having an extended source display a flatter distribution, falling off more slowly with ρ (e.g., see Figure 3 in Dello Russo et al. 1998 and Figure 5 in Dello Russo et al. 2016a). By summing the spatial profiles of all individual lines for each species within a grating setting, we were able to extract spatial profiles for emission from H_2O, CH_3OH, HCN, OH^*, and C_2H_6 in ER61 (see Figure 2).

There is a slight asymmetry in the dust profile on April 16 and on May 12–13. Our measurements may suggest a consistent enhancement in the sunward direction of H_2O and C_2H_6 compared to the dust profile on May 11. The signal-to-noise ratio is not sufficient to say with certainty whether CH_3OH also follows this trend. The profiles for dust and all molecules track one another, suggesting that molecules are coreleased.

4.2. Molecular Fluorescence Analysis

Synthetic models of fluorescence emission for each targeted species were compared to observed line intensities, after correcting each modeled line intensity (g-factor) for the monochromatic atmospheric transmittance at its Doppler-shifted wavelength (according to the geocentric velocity of the comet at the time of the observations). The g-factors used in synthetic emission models in this study were generated with quantum mechanical models developed for H_2O (Villanueva et al. 2012a), OH^* (Bonev et al. 2006), C_2H_6 (Villanueva et al. 2011b), CO, C_2H_2, and CH_4 (Gibb et al. 2003; Villanueva et al. 2011a; Paganini et al. 2013), NH_3, HCN (Lippi et al. 2013;

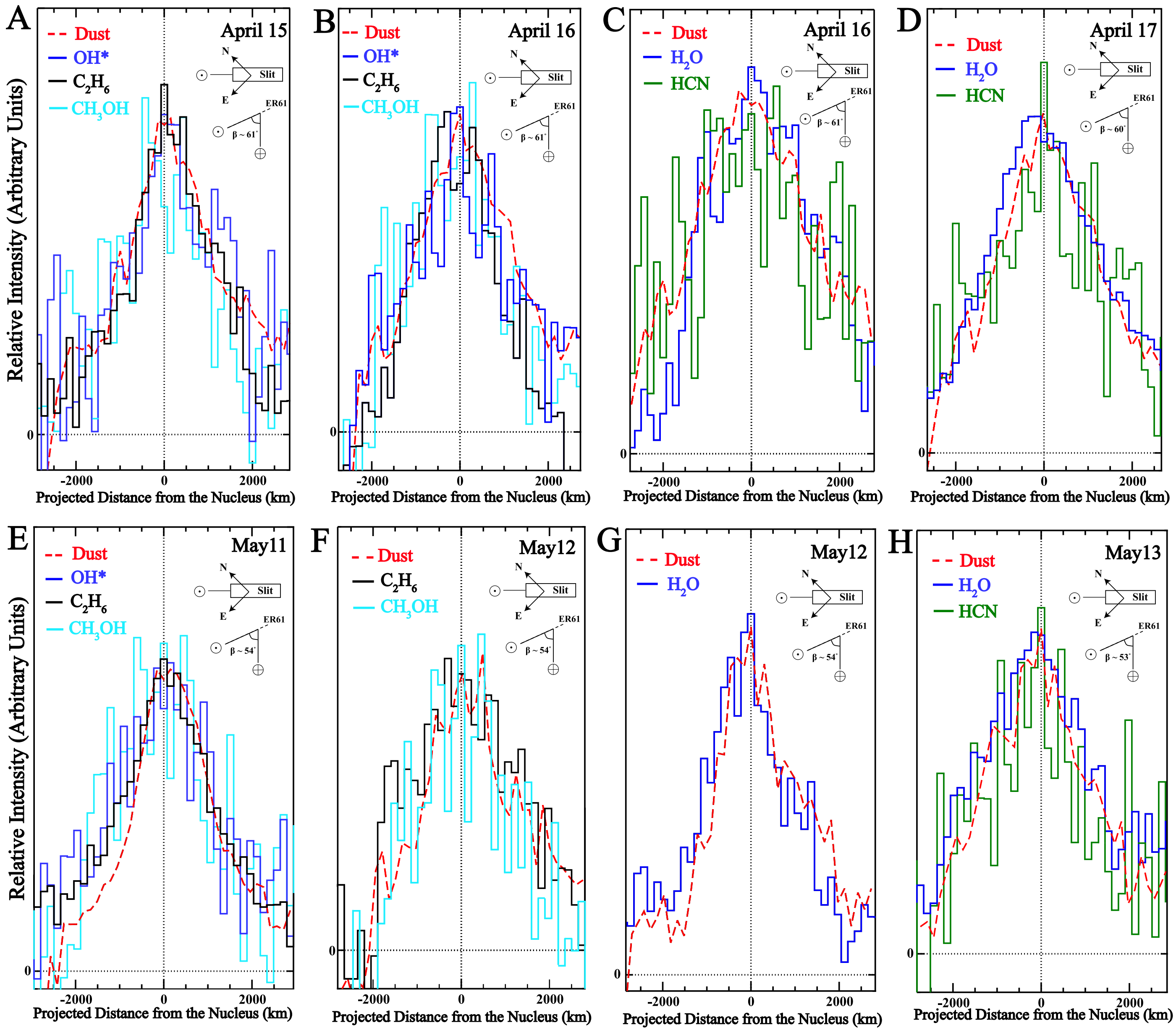

Figure 2. Panels A–H show spatial profiles of multiple volatiles simultaneously measured with dust (red dashed line) in comet ER61 spanning UT 2017 April 15 to May 13. The slit was oriented along the projected Sun–comet line (position angle ∼252°), with the Sun-facing direction to the left as indicated. The Sun–comet–Earth angle (phase angle, β) is also shown in each panel for each date.

Villanueva et al. 2013), H_2CO (DiSanti et al. 2006), and CH_3OH (Villanueva et al. 2012b; DiSanti et al. 2013). Production rates for each sampled species were determined from the appropriate fluorescence model at the best-fit rotational temperature of each molecule (see Section 4.3).

A line-by-line analysis and a Levenberg–Marquardt nonlinear minimization technique (Villanueva et al. 2008) was used to fit fluorescence emission from all species simultaneously within each echelle order, allowing for high-precision results, even in spectrally crowded regions containing many spectral lines within a single instrumental resolution element.

4.3. Determination of Rotational Temperature

Rotational temperatures ($T_{\rm rot}$) were determined using correlation and excitation analyses that have been extensively described in the literature (e.g., Bonev 2005; DiSanti et al. 2006; Bonev et al. 2008; Villanueva et al. 2008). In general, well-constrained rotational temperatures can be determined for individual species with intrinsically bright lines and for which a sufficiently broad range of excitation energies is sampled. These conditions are met for several molecules in multiple iSHELL orders, including strong H_2O lines in Lcustom order 179 with iSHELL spanning ∼3437.8–3465.8 $\rm cm^{-1}$; these are augmented by including other H_2O lines in additional iSHELL orders (see Figure 1 and Table 2).

We found consistent rotational temperatures for several molecules on all of our dates. The $T_{\rm rot}$ for CH_3OH was well constrained on April 15 (78 ± 8 K) and was consistent (within uncertainty) with those for C_2H_6 and H_2CO on the same date, and with those of HCN, CH_3OH, and H_2O on April 16 and 17 (see Table 2). Rotational temperatures for our May dates were also in agreement, being 61 ± 8 K and 63^{+13}_{-11} K for CH_3OH on May 11 and May 12, 60^{+6}_{-5} K and 61^{+11}_{-8} K for H_2O on May 12

Table 2
Molecular Species Measured in Comet ER61

iSHELL Setting	Molecule	T_{rot}[a] (K)	GF[b]	Q[c] (molecules s^{-1})	Q_x/Q_{H2O}[d] (%)	Q_x/Q_{C2H6}[e]
2017 April 15, R_h = 1.11 AU, Δ = 1.18 AU, $d\Delta/dt$ = −2.39 km s^{-1}						
Lp1	OH^*(f)	(78)	2.37 ± 0.20	$(1.22 \pm 0.17) \times 10^{29}$	100	156 ± 27
	CH_3OH	78 ± 8	2.33 ± 0.32	$(3.22 \pm 0.15) \times 10^{27}$	2.63 ± 0.45	4.13 ± 0.47
	H_2CO	(78)	(237)	$(4.50 \pm 0.88) \times 10^{26}$	0.36 ± 0.11	0.57 ± 0.13
		74^{+25}_{-19}	(237)	$(4.39 \pm 0.85) \times 10^{26}$	0.35 ± 0.10	0.56 ± 0.12
	C_2H_6	78^{+12}_{-10}	2.37 ± 0.15	$(7.89 \pm 0.24) \times 10^{26}$	0.64 ± 0.11	1
2017 April 16, R_h = 1.11 AU, Δ = 1.17 AU, $d\Delta/dt$ = −1.25 km s^{-1}						
Lcustom	H_2O	75 ± 4	2.27 ± 0.16	$(6.50 \pm 0.31) \times 10^{28}$	100	152 ± 17
	C_2H_2	(75)	(227)	$<7.28 \times 10^{25}$	<0.11(g)	<0.17
	HCN	68^{+27}_{-20}	(227)	$(8.76 \pm 0.8) \times 10^{25}$	0.14 ± 0.02	0.20 ± 0.03
		(75)	(227)	$(9.05 \pm 0.91) \times 10^{25}$	0.13 ± 0.02	0.21 ± 0.03
	HC_3N	(75)	(227)	$<1.32 \times 10^{25}$	<0.02(g)	<0.03
	NH_3	(75)	(227)	$<4.99 \times 10^{26}$	<0.76(g)	<1.17
Lp1[h]	CH_3OH	(75)	(227)	$(2.24 \pm 0.07) \times 10^{27}$	3.44 ± 0.40	5.25 ± 0.58
		68 ± 8	(227)	$(2.06 \pm 0.06) \times 10^{27}$	3.17 ± 0.36	4.83 ± 0.53
	H_2CO	(75)	(227)	$(2.08 \pm 0.15) \times 10^{26}$	0.32 ± 0.11	0.48 ± 0.06
	C_2H_6	(75)	(227)	$(4.26 \pm 0.15) \times 10^{26}$	0.65 ± 0.07	1.00
2017 April 17, R_h = 1.10 AU, Δ = 1.17 AU, $d\Delta/dt$ = −1.19 km s^{-1}						
Lcustom	H_2O	74^{+6}_{-5}	2.34 ± 0.12	$(1.07 \pm 0.03) \times 10^{29}$	100	N/A
	C_2H_2	(74)	(234)	$(1.39 \pm 0.37) \times 10^{26}$	0.13 ± 0.04(i)	N/A
	HCN	87^{+15}_{-17}	(234)	$(1.22 \pm 0.16) \times 10^{26}$	0.11 ± 0.02	N/A
		(74)	(234)	$(1.18 \pm 0.15) \times 10^{26}$	0.11 ± 0.02	N/A
	HC_3N	(74)	(234)	$<1.45 \times 10^{25}$	<0.01(g)	N/A
	NH_3	(74)	(234)	$(7.47 \pm 1.40) \times 10^{26}$	0.70 ± 0.14	N/A
2017 May 11, R_h = 1.04 AU, Δ = 1.24 AU, $d\Delta/dt$ = 9.00 km s^{-1}						
Lp1	OH^*(f)	(61)	2.21 ± 0.20	$(7.22 \pm 0.95) \times 10^{28}$	100	174 ± 32
	CH_3OH	61 ± 8	(221)	$(2.12 \pm 0.15) \times 10^{27}$	2.94 ± 0.79	5.10 ± 0.75
	H_2CO	(61)	(221)	$(2.03 \pm 0.63) \times 10^{26}$	0.28 ± 0.09	0.48 ± 0.16
		67^{+28}_{-19}	(221)	$(2.18 \pm 0.66) \times 10^{26}$	0.30 ± 0.11	0.52 ± 0.17
	CH_4	(61)	(221)	$<4.81 \times 10^{27}$	<0.89 (g)	<11.6
	C_2H_6	55^{+18}_{-13}	(2.25 ± 0.20)	$(4.07 \pm 0.33) \times 10^{26}$	0.56 ± 0.15	N/A
		(61)	(221)	$(4.15 \pm 0.34) \times 10^{26}$	0.57 ± 0.15	1.00
2017 May 12, R_h = 1.04 AU, Δ = 1.25 AU, $d\Delta/dt$ = 9.25 km s^{-1}						
M2(j)	H_2O	60^{+6}_{-5}	2.34 ± 0.36	$(7.04 \pm 0.25) \times 10^{28}$	100	283 ± 34
	OCS	(60)	(234)	$(1.06 \pm 0.19) \times 10^{26}$	0.15 ± 0.03	0.42 ± 0.09
	CO	(60)	(234)	$<4.44 \times 10^{26}$	<0.63(g)	<1.79
Lp1(h)	CH_3OH	(60)	(234)	$(1.42 \pm 0.10) \times 10^{27}$	2.02 ± 0.26	5.72 ± 0.77
		63^{+13}_{-11}	(234)	$(1.38 \pm 0.13) \times 10^{27}$	1.96 ± 0.28	5.56 ± 0.82
	H_2CO	(60)	(234)	$(8.40 \pm 1.77) \times 10^{25}$	0.12 ± 0.03	0.34 ± 0.08
	CH_4	(60)	(234)	$<4.01 \times 10^{26}$	<0.57(h)	<1.61
	C_2H_6	(60)	(234)	$(2.48 \pm 0.14) \times 10^{26}$	0.35 ± 0.04	1.00
2017 May 13, R_h = 1.04 AU, Δ = 1.25 AU, $d\Delta/dt$ = 9.70 km s^{-1}						
Lcustom	H_2O	61^{+11}_{-8}	2.19 ± 0.15	$(3.98 \pm 0.45) \times 10^{28}$	100	N/A
	C_2H_2	(61)	(219)	$(2.87 \pm 0.19) \times 10^{25}$	0.07 ± 0.01	N/A
	HCN	57 ± 9	(219)	$(4.30 \pm 0.33) \times 10^{25}$	0.10 ± 0.02	N/A
		(61)	(219)	$(4.62 \pm 0.83) \times 10^{25}$	0.11 ± 0.02	N/A
	HC_3N	(61)	(219)	$<5.20 \times 10^{24}$	<0.04(g)	N/A
	NH_3	(61)	(219)	$(1.51 \pm 0.29) \times 10^{26}$	0.37 ± 0.09	N/A

Notes.

[a] Rotational temperature. Values in parentheses are assumed.

[b] Growth factor. Values in parentheses are assumed.

[c] Global production rate. Errors in production rate include line-by-line deviation between modeled and observed intensities and photon noise (see Dello Russo et al. 2004; Bonev 2005; Bonev et al. 2007).

[d] Molecular abundance with respect to H_2O.

[e] Abundance ratios with respect to C_2H_6 (for dates on which C_2H_6 was measured).

[f] OH^* (OH prompt emission) used as a proxy for H_2O.

[g] 3σ upper limit.

[h] The GF of CH_3OH (2.50 ± 0.38) on April 16 was in agreement with that of H_2O. For CH_3OH and C_2H_6, the GF was 2.19 ± 0.36 and 2.38 ± 0.20 on May12 respectively; thus, we assumed the GF of H_2O when calculating Qs and mixing ratios for those molecules.

[i] 4σ detection.

[j] Values for H_2O and OCS are from Saki et al. (2020a).

(Saki et al. 2020a) and May 13, respectively. The $T_{\rm rot}$ derived for other molecules were in formal agreement with those of H_2O in ER61 (see Table 2); however, we adopted the rotational temperature of simultaneously measured H_2O (or CH_3OH and C_2H_6 in the Lp1 setting with no H_2O emission lines) within the same setting for species without a well-constrained $T_{\rm rot}$ (C_2H_2, NH_3, OCS, CO, CH_4, HC_3N). Although ER61 was slightly closer to the Sun in May (1.04 AU) compared with April (1.11 AU), our measurements are consistent with a higher $T_{\rm rot}$ in April compared with May, perhaps owing to the higher production rates (Qs) of volatiles in the coma in April resulting from the recent outburst (Wesołowski et al. 2020). Higher production rates and $T_{\rm rot}$ have also been observed in other outbursting comets (see Sekanina 2010, 2017 and references therein). Rotational temperatures for different molecules for the same comet and within the same instrumental setting are generally found to be consistent, even for molecules with differing photodissociation lifetimes (e.g., see Bonev 2005; DiSanti et al. 2006; Gibb et al. 2012; DiSanti et al. 2016; supporting this approach).

4.4. Production Rates and Mixing Ratios

Production rates for sampled species were determined using the appropriate fluorescence model at the measured (or assumed) rotational temperature. Nucleus-centered production rates (Q_{NC}, molecules s^{-1}) were calculated using the well-established formalism relating line flux, fluorescence g-factor, and physical (gas outflow speed, photodissociation lifetime) and geometric parameters (R_h, Δ; see Dello Russo et al. 1998; DiSanti et al. 2001; Bonev 2005; DiSanti et al. 2006, 2014). $Q_{\rm NC}$ is then scaled by a growth factor (GF), which relates molecular production rates in regions of the coma along the column included in the beam (of size $0''.75 \times 2''.5$) to the global production rate ($Q_{\rm global}$). This method analyzes spatial profiles of emission using the "Q-curve" formalism, dating back to the analysis of OCS in comet Hale-Bopp (Dello Russo et al. 1998). A canonical spherically symmetric outflow velocity, $v_{\rm gas} = 800\ R_h^{-0.5}$ m s^{-1}, was assumed in determining our production rates. This velocity is based on velocity-resolved observations of several moderately bright comets at radio wavelengths (Biver et al. 2006; Cordiner et al. 2014 also see Bonev 2005 supporting this assumption).

When calculating production rates, we assumed the GF of simultaneously measured OH^* (proxy for H_2O, when water is not sampled) on April 15 and May 11 (consistent with the GF measured for C_2H_6 and CH_3OH on April 15 and with C_2H_6 on May 11) and of H_2O on April 16–17 and on May 12–13. This is supported by their similar profiles (see Figure 2). Global production rates for all the targeted species and their mixing ratios relative to water are presented in Table 2. Figures 3(A)–(B) show sampled extracted spectra with clear emissions from many volatiles in comet ER61 (with traces and labels as described in Figure 1).

Using alternative compositional baselines other than H_2O (Qx/$Q_{\rm H2O}$ %) can provide richer insights in comparing comets. For instance, Biver & Bockelée-Morvan (2019) used CH_3OH as their measurement baseline in comparing complex organic molecules in comets. Owing to the low vacuum sublimation temperature of C_2H_6, distinct outgassing morphologies in many comets compared with H_2O, and the easy detectability of this molecule at near-IR wavelengths, C_2H_6 can serve as a possible alternative compositional baseline (see Section 5.4.2 in Bonev et al. 2021 for details). Therefore, we present abundances with respect to both H_2O and C_2H_6 (when we have C_2H_6 detection available; see Table 2).

5. Discussion

5.1. Variability of Production Rates and Mixing Ratios

The nucleus of ER61 was estimated to be ∼10 km in radius (Meech et al. 2017). Its geocentric distance and obscuration by the bright coma make it impossible to directly measure individual surface sublimation regions. However, as a comet rotates, different sublimation regions of the nucleus are activated and may give rise to short-term variability in production rates or (in the case of a heterogeneous nucleus) mixing ratios (e.g., Hässig et al. 2015; Roth et al. 2018).

We saw clear variability in production rates of most species over the course of our ER61 observations (UT 2017 April 15—May 13). The production rates of H_2O, CH_3OH, C_2H_6, and H_2CO decreased from April 15 to April 16, followed by an increase in the production rates of H_2O, NH_3, C_2H_2, and HCN from April 16 to 17, whereas the 3σ upper limits for HC_3N were consistent. CH_3OH, C_2H_6, and H_2CO were not targeted on April 17, making it difficult to compare their production rates with those on April 16. We observed a clear decrease in the production rates of some volatile species from April 17 to May 11 (near perihelion) through May 13 (post-perihelion; see Figure 4). Our measured abundances indicate that (within uncertainties) the mixing ratios of CH_3OH, C_2H_6, H_2CO, HCN, NH_3, and C_2H_2 remained consistent from three-plus weeks pre-perihelion to near perihelion (May 11), whereas abundances of all volatile species except CH_3OH, HCN, and the 3σ upper limit for HC_3N decreased post-perihelion (May 12–13). ER61 was more volatile poor (with respect to H_2O) post- versus pre-perihelion. This could be because of its recent outburst on April 4 (close to our April observations). Outbursts release more material from subsurface areas of the nucleus that may be more volatile rich, causing a possible variability in the production rates and mixing ratios of volatiles similar to those seen in ER61.

Chemically heterogeneous sources on the nucleus, dominating volatile release at different times owing to seasonal effects, may be the most plausible cause for the observed pre- versus post-perihelion variability in ER61. Such asymmetries with respect to perihelion are observed in some previous comets, including 2P/Encke (A'Hearn et al. 1985; Roth et al. 2018), 67P (e.g., Hässig et al. 2015; Le Roy et al. 2015), and C/2009 P1 (Garradd; Bodewits et al. 2014; McKay et al. 2015).

The Rosetta mission to comet 67P found that mixing ratios of some species (e.g., CO, CO_2, OCS) varied owing to seasonal effects on the nucleus (Hässig et al. 2015). In comet C/2009 P1 (Garradd) the production rate of CO increased even after the comet passed perihelion, perhaps owing to the existence of seasonal effects, whereas the production rate of H_2O followed the predicted heliocentric dependence (decreasing as the comet passed perihelion, Bodewits et al. 2014; McKay et al. 2015). The depleted CH_3OH reported during 2P/Encke's 2017 apparition (Roth et al. 2018) compared with its enriched abundance in 2003 (Radeva et al. 2013), plus other compositional differences observed in 2017 compared to 2003, may also have resulted from seasonal effects (see Roth et al. 2018 for a detailed discussion of seasonal effects on the volatile content of comets).

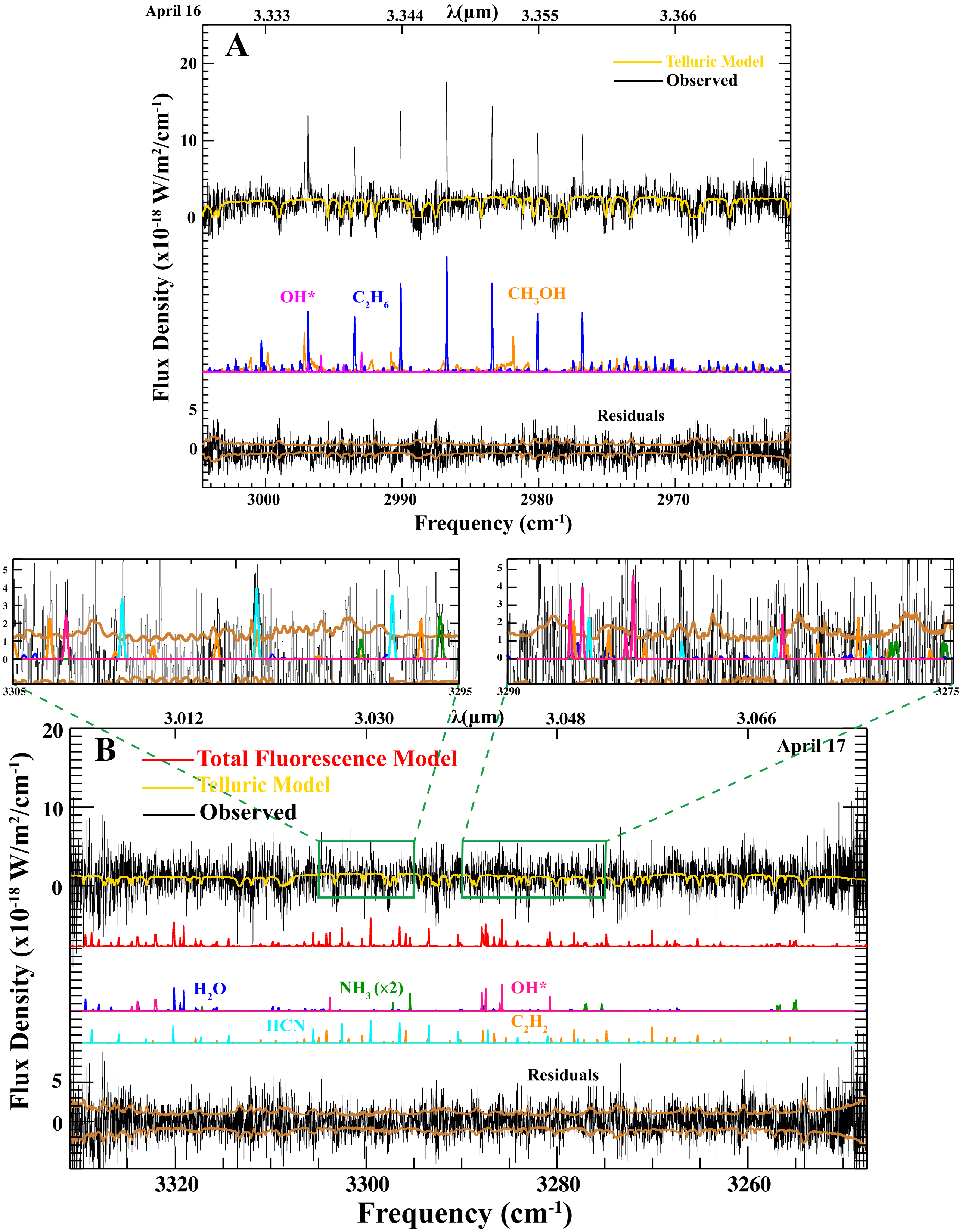

Figure 3. Panels A–B show fluorescence emission of multiple species in comet ER61 on UT 2017 April 16 and 17, respectively. The yellow traces overplotted on the uppermost cometary spectra are the telluric absorption models (convolved to the instrumental resolution). Individual fluorescence emission models (color-coded by species for clarity) are plotted below. At the bottom of each panel is the residual spectrum (after subtracting the telluric absorption model and all relevant fluorescent emission models) with the 1σ uncertainty envelope overplotted in bronze. The zoomed subplot in panel B highlights the location and intensity of emission lines of many volatiles with respect to the 1σ uncertainty envelope plotted in bronze; each subplot has the same units as the larger plot.

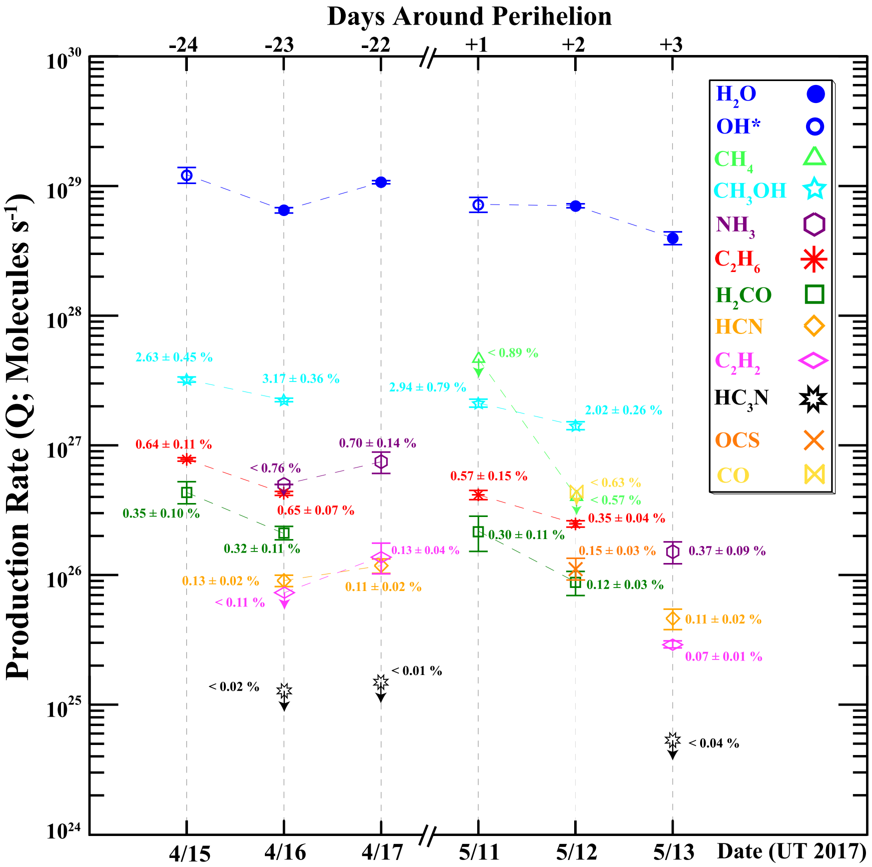

Figure 4. Production rates and mixing ratios (in percent relative to H_2O) of trace species sampled on multiple dates in ER61, showing the variability of production rates and mixing ratios of some volatile species on short and long-timescales.

5.2. The 3σ Upper Limit of HC_3N

The improved sensitivity and spectral coverage of iSHELL allowed us to measure or constrain molecules that we previously could not, such as HC_3N, which has been suggested as a possible parent for CN (e.g., Fray et al. 2005; Bockelée-Morvan & Crovisier 1985). HC_3N has been observed via radio wavelengths in many comets (with mixing ratios ranging from 0.002% to 0.07% with respect to H_2O). Upper limits for HC_3N have also been reported in many comets, including comet 46P/Wirtanen during its 2018 apparition with an abundance of <0.007% (the most stringent upper limit to date at near-IR wavelengths; Khan et al. 2021), similar to its abundance in comet 1P/Halley (see Bockelée-Morvan et al. 1987; Khan et al. 2021). Crovisier et al. (1993) reported a 3σ upper limit of <0.00019% in radio observations of comet Levy 1990 XX (the lowest abundance yet reported in any comet). In ER61, combining the unblended HC_3N lines (see Figure 5) enabled us to achieve a sensitive 3σ upper limit (<0.02%, averaged over three days), similar to those reported for comets C/2009 P1 (Garradd) (<0.03%; Villanueva et al. 2012a) and 103P/Hartley 2 (<0.024%; Dello Russo et al. 2011).

5.3. Comparison with Other OCCs

Compared to mean abundances among OCCs characterized to date at near-IR wavelengths (Dello Russo et al. 2016a), our measurements in ER61 indicate that CH_3OH was enriched pre-perihelion and "typical" post-perihelion. HCN was slightly depleted both pre- and post-perihelion. NH_3, H_2CO, C_2H_2, and C_2H_6 were typical pre-perihelion and slightly depleted post-perihelion, whereas OCS was typical (see Table 3 and Figure 6; also see Figure 5 in Saki et al. 2020a and Table 8 in Dello Russo et al. 2016a).

With the large spectral grasp of iSHELL, many of the trace molecules reported here were observed simultaneously (and with H_2O and/or OH*) within a single iSHELL setting. This is not necessarily the case for comets observed with other near-IR spectrographs that represent the current database of IR observations used to delineate abundance categories, and the effects of nonsimultaneous measurements of H_2O and other trace species must be considered when interpreting mixing ratios (Dello Russo et al. 2016a). Early results obtained at near-IR wavelengths suggested three taxonomic classes: (1) organics-depleted, (2) organics-normal, and (3) organics-enriched (Mumma & Charnley 2011), but additional observations have revealed comets that do not fit neatly into these taxonomic classes (i.e., comets can be depleted in certain volatiles while enriched in others; e.g., Gibb et al. 2012; Radeva et al. 2013; Dello Russo et al. 2016a; Roth et al. 2017). Recently, new (and still evolving) taxonomic classes and volatile relationships in comets have been suggested (see Dello Russo et al. 2016a for details). The overall weighted averages in ER61 indicate that it is enriched in CH_3OH, consistent with average in OCS (Saki et al. 2020a) and depleted in the remaining volatiles (see Figure 6). The pre- to post-perihelion variation in relative abundances makes it difficult to classify ER61, though it has the most compositional similarities on its pre-perihelion dates to comet 2P/Encke and on post- perihelion dates to comet C/2012 S1 ISON when it was at $R_h \geqslant 0.83$ AU (Dello Russo et al. 2016a and references therein). Table 3 shows mean primary volatile abundance ratios (for species with more than a

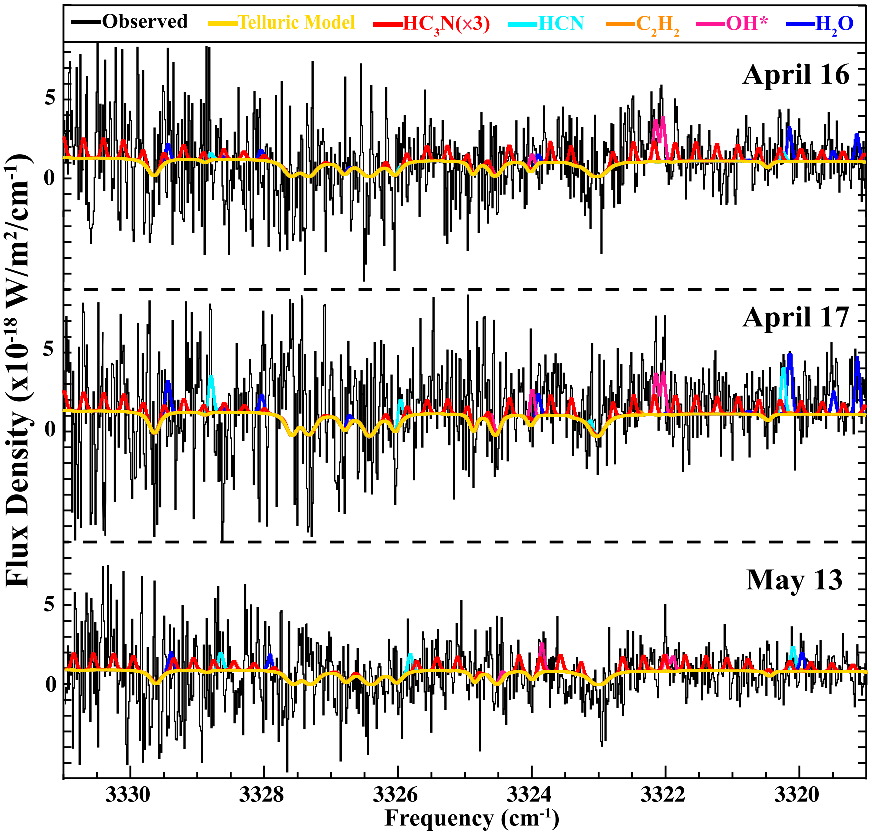

Figure 5. Fluorescence emissions of cyanoacetylene (HC_3N) centered around 3325 cm^{-1} on UT 2017 April 16 and 17, and May 13. The yellow traces overplotted on the uppermost cometary spectra are the telluric absorption models (convolved to the instrumental resolution). Individual fluorescence emission models (color-coded by species for clarity) are overplotted.

Table 3
ER61 Mean Abundances for Molecules with More than a Single Measurement

Molecule	Pre-perihelion Abundance[a] (%)	Near-perihelion Abundance[b] (%)	Post-perihelion Abundance[c] (%)	Overall Weighted Mean in ER61 (%)	OCC Average[d] (%)
C_2H_2	0.13 ± 0.04	...	0.07 ± 0.01	0.07 ± 0.01	0.16 ± 0.03
HCN	0.12 ± 0.01	...	0.11 ± 0.02	0.12 ± 0.01	0.22 ± 0.03
NH_3	0.70 ± 0.15	...	0.37 ± 0.09	0.45 ± 0.07	0.91 ± 0.30
H_2CO	0.34 ± 0.06	0.30 ± 0.09	0.12 ± 0.03	0.19 ± 0.02	0.33 ± 0.08
CH_3OH	3.11 ± 0.23	2.94 ± 0.79	2.02 ± 0.26	2.64 ± 0.17	2.21 ± 0.24
C_2H_6	0.64 ± 0.06	0.57 ± 0.15	0.35 ± 0.04	0.44 ± 0.03	0.63 ± 0.10

Notes. In calculating the mean abundances, we have excluded the 3σ upper limits for species with both detections and upper limits as reported in this work (see Table 2.).

[a] Weighted mean of all the pre-perihelion measurements.

[b] Near-perihelion measurements on May 11.

[c] OCS (Saki et al. 2020a), CO, and CH_4 (upper limits) were only measured on May dates (see Table 2), so these species have been excluded from this table.

[d] Averages among all OCCs from Dello Russo et al. (2016a).

single measurement) in ER61 on pre-perihelion, near-perihelion, and post-perihelion dates and the mean abundances among OCCs.

6. Summary

We characterize ER61 primary volatile composition and spatial associations using iSHELL at NASA-IRTF on UT 2017 April 15–17 (shortly after its April 4 outburst) and on May 11–13. Our measurements indicate the following results:

1. We obtained production rates and mixing ratios with respect to H_2O (and C_2H_6 when a C_2H_6 measurement was available) of the primary volatiles CH_3OH, HCN, C_2H_2, NH_3, H_2CO, OCS, and obtained a stringent 3σ upper limit for CO, CH_4, and HC_3N.
2. We were able to extract spatial profiles for H_2O, C_2H_6, CH_3OH, OH*, HCN, and comeasured dust on pre-perihelion, near-perihelion, and post-perihelion dates. These profiles might suggest a slight asymmetric outgassing of

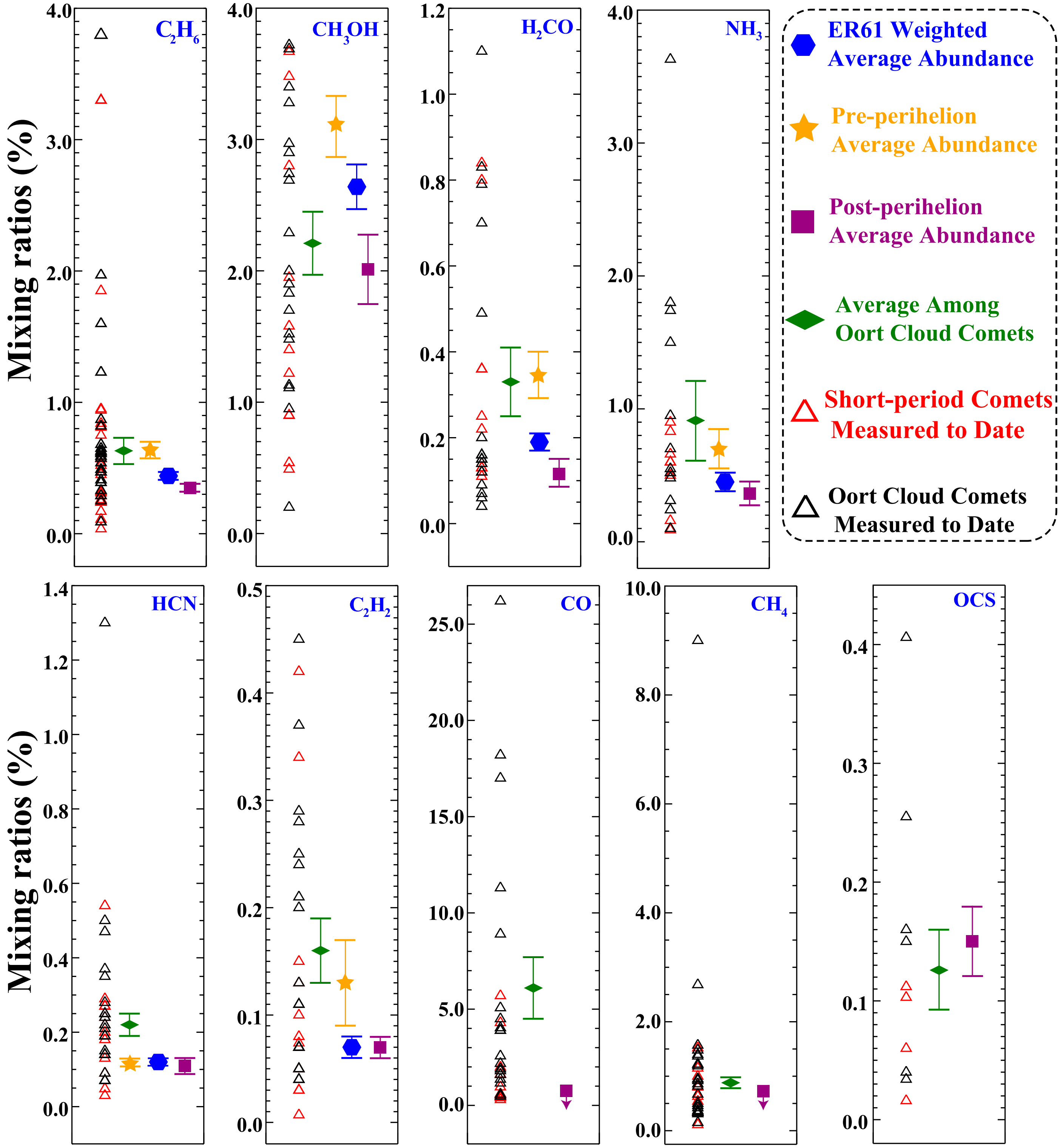

Figure 6. Comparison of mixing ratios of volatiles sampled in ER61 (this work) with the near-IR measurements of each volatile in OCCs (black) and ecliptic (short-period) comets (red) measured to date, as well as the respective mean values for each volatile among OCCs in green (Dello Russo et al. 2016a; Dello Russo et al. 2020; DiSanti et al. 2017; Roth et al. 2020; Faggi et al. 2018; Saki et al. 2020a; Roth et al. 2017, 2018). Error bars indicate 1σ uncertainties on detections, whereas downward arrows indicate 3σ upper limits (for hypervolatiles CO and CH_4). Note that for plotting purposes we have excluded the highly enriched CO comets such as C/2016 R2 (PanSTARRS; Biver et al. 2018; McKay et al. 2019) and C/2010 G2 Hill (Kawakita et al. 2014) with >100% CO content relative to H_2O.

dust on April 16 and May 13. Our measurements on May 11 suggest a consistent enhancement in the sunward direction of H_2O and C_2H_6 compared to the dust profile. Owing to a low signal-to-noise ratio, it is not clear if CH_3OH follows this trend.

3. We found that ER61 exhibits short-term (day-to-day) and long-term (pre- versus post-perihelion) variability, perhaps owing to its outburst on April 4 (shortly before our April measurements) or seasonal effects along its orbit similar to the variability seen in comets 2P/Encke and 67P/C-G.

4. We placed the chemical composition of ER61 in the context of other OCCs measured to date at near-IR wavelengths and found that ER61 is overall enriched in CH_3OH, consistent with the average in OCS, and depleted in the remaining volatiles. The pre- to post-perihelion variation in relative abundances makes it difficult to classify ER61, though it has the most compositional similarities on its pre-perihelion dates to comet 2P/Encke and on post- perihelion dates to comet C/2012 S1 ISON when it was at $R_h \geqslant 0.83$ AU. Differences in observational circumstances, techniques, and instruments need to be considered in order to better compare properties between comets within the population.
5. Our ER61 measurements indicate the necessity of comet volatile measurements in both short (day-to-day) and long (pre- versus post-perihelion) timescales to address the "snapshot" bias associated with cometary observations taken over a limited range of dates and/or heliocentric distances.

Data for this study were obtained at the NASA Infrared Telescope Facility (IRTF), operated by the University of Hawai'i under contract NNH14CK55B with the National Aeronautics and Space Administration (NASA). We are most fortunate to have the opportunity to conduct observations from Maunakea and recognize and acknowledge the very significant cultural role and reverence that the summit of Maunakea has always had within the indigenous Hawaiian community. This study was generously funded by the NASA Planetary Astronomy/Solar System Observations (NNX12AG24G, 15-SSO15_2-0028, 18-SSO18_2-0040, 80NSSC17K0705), Solar System Workings (NNX17AC86G), and Emerging Worlds (80NSSC20K0341) Programs, the NASA Astrobiology Institute (13-13NAI7_2_0032), the National Science Foundation (AST-2009398, AST-2009910, AST-1616306, AST-1615441), and NASA Headquarters under the NASA Earth and Space Science Fellowship Program (grant NNX16AP49H). We acknowledge and thank the entire staff at IRTF for their support during our observations.

ORCID iDs

Mohammad Saki https://orcid.org/0000-0003-2277-6232
Erika L. Gibb https://orcid.org/0000-0003-0142-5265
Boncho P. Bonev https://orcid.org/0000-0002-6391-4817
Nathan X. Roth https://orcid.org/0000-0002-6006-9574
Michael A. DiSanti https://orcid.org/0000-0001-8843-7511
Younas Khan https://orcid.org/0000-0003-4773-2674
Ronald J. Vervack Jr. https://orcid.org/0000-0002-8227-9564
Adam J. McKay https://orcid.org/0000-0002-0622-2400
Hideyo Kawakita https://orcid.org/0000-0003-2011-9159

References

A'Hearn, M. F. 2017, RSPTA, 375, 20160261
A'Hearn, M. F., Birch, P. V., Feldman, P. D., et al. 1985, Icar, 64, 1
A'Hearn, M. F., Millis, R. C., Schleicher, D. O., et al. 1995, Icar, 118, 223
Biver, N., & Bockelée-Morvan, D. 2019, ACS Earth and Space Chemistry, 3, 1550
Biver, N., Bockelée-Morvan, D., Crovisier, J., et al. 2006, A&A, 449, 1255
Biver, N., Bockelée-Morvan, D., Moreno, R., et al. 2015, SciA, 1, e1500863
Biver, N., Bockelée-Morvan, D., Paubert, G., et al. 2018, A&A, 619, A127
Bockelée-Morvan, D., & Crovisier, J. 1985, AAP, 151, 90
Bockelée-Morvan, D., Crovisier, J., & Despois, D. 1987, AAP, 180, 253
Bockelée-Morvan, D., Crovisier, J., Erard, S., et al. 2016, MNRAS, 462, S1270
Bockelée-Morvan, D., Crovisier, J., Mumma, M. J., et al. 2004, in Comets II, ed. M. C. Festou, H. U. Keller, & H. A. Weaver (Tucson, AZ: Univ. Arizona Press), 391
Bockelée-Morvan, D., Lis, D. C., Wink, J. E., et al. 2000, A&A, 353, 1101
Bodewits, D., Farnham, T. L., & A'Hearn, M. F. 2014, ApJ, 786, 48
Bonev, B. P. 2005, PhD thesis, Univ. Toledo, http://astrobiology.gsfc.nasa.gov/Bonev_thesis.pdf
Bonev, B. P., Dello Russo, N. D., DiSanti, M. A., et al. 2021, PSJ, 2, 45
Bonev, B. P., Mumma, M. J., DiSanti, M. A., et al. 2006, ApJ, 653, 774
Bonev, B. P., Mumma, M. J., Kawakita, H., et al. 2008, Icar, 196, 241
Bonev, B. P., Mumma, M. J., Villanueva, G. L., et al. 2007, ApJ, 661, L97
Brooke, T. Y., Weaver, H. A., Chin, G., et al. 2003, Icar, 166, 167
Chubko, L. S., Churyumov, K. I., Lukýanyk, I. V., & Guliev, A. S. 2005, HiA, 13, 768
Clements, T. D., & Fernandez, Y. 2021, AJ, 161, 73
Cochran, A. L., Levasseur-Regourd, A.-C., Cordiner, M., et al. 2015, SSRv, 197, 9
Cordiner, M. A., Remijan, A. J., Boissier, J., et al. 2014, ApJL, 792, L2
Crovisier, J., Bockelée-Morvan, D., Colom, P., et al. 1993, AAP, 269, 527
Dello Russo, N., Bonev, B. P., DiSanti, M. A., et al. 2005, ApJ, 621, 537
Dello Russo, Neil, DiSanti, Michael A, Magee-Sauer, Karen, et al. 2004, Icar, 168, 186
Dello Russo, N., DiSanti, M. A., Mumma, M. J., Magee-Sauer, K., & Rettig, T. W. 1998, Icar, 135, 377
Dello Russo, N., Kawakita, H., & Bonev, B. P. 2020, Icar, 335, 113411
Dello Russo, N., Kawakita, H., Vervack, R. J., Jr., & Weaver, H. A. 2016a, Icar, 278, 301
Dello Russo, N., Vervack, R. J., Jr., Kawakita, H., et al. 2016b, Icar, 266, 152
Dello Russo, N., Vervack, R. J., Jr., Lisse, C. M., et al. 2011, ApJL, 734, L8
DiSanti, M. A., Bonev, B. P., Dello Russo, N., et al. 2017, AJ, 154, 246
DiSanti, M. A., Bonev, B. P., Gibb, E. L., et al. 2016, ApJ, 820, 34
DiSanti, M. A., Bonev, B. P., Magee-Sauer, K., et al. 2006, ApJ, 650, 470
DiSanti, M. A., Bonev, B. P., Villanueva, G. L., et al. 2013, ApJ, 763, 19
DiSanti, M. A., Mumma, M. J., Dello Russo, N., & Magee-Sauer, K. 2001, Icar, 153, 361
DiSanti, M. A., Villanueva, G. L., Paganini, L., et al. 2014, Icar, 228, 167
El-Maarry, M. R., Groussin, O., Thomas, N., et al. 2017, LPSC, 2017, 2791
Faggi, S., Villanueva, G. L., Mumma, M. J., & Paganini, L. 2018, AJ, 156, 68
Fray, N., Bénilan, Y., Cottin, H., et al. 2005, PLANSS, 53, 1243
Gibb, E. L., Bonev, B. P., Villanueva, G. L., et al. 2012, ApJ, 750, 102
Gibb, E. L., Mumma, M. J., Dello Russo, N., et al. 2003, Icar, 165, 391
Gomes, R., Levison, H. F., Tsiganis, K., & Morbidelli, A. 2005, Natur, 435, 466
Gronkowski, P. 2002, P&SS, 50, 247
Gronoff, G., Maggiolo, R., Cessateur, G., et al. 2020, ApJ, 890, 89
Hässig, M., Altwegg, K., Balsiger, H., et al. 2015, Sci, 347, aaa0276
Kawakita, H., Dello Russo, N., & Vervack, R. Jr. 2014, ApJ, 788, 110
Khan, Y., Gibb, E. L., Bonev, B. P., et al. 2021, PSJ, 2, 20
Kobayashi, H., Kawakita, H., Mumma, M. J., et al. 2007, ApJL, 2007, L75
Le Roy, L., Altwegg, K., Balsiger, H., et al. 2015, A&A, 583, A1
Levison, H. F., Morbidelli, A., Tsiganis, K., et al. 2011, AJ, 142, 152
Lippi, M., Villanueva, G. L., DiSanti, M. A., et al. 2013, A&A, 551, A51
McKay, A. J., Cochran, A. L., DiSanti, M. A., et al. 2015, Icar, 250, 504
McKay, A. J., DiSanti, M. A., Kelley, M. S. P., et al. 2019, AJ, 158, 128
Meech, K. J., Schambeau, C. A., Sorli, J. T., et al. 2017, AJ, 153, 206
Mumma, M. J., & Charnley, S. B. 2011, ARA&A, 49, 471
Nesvorný, D., Vokrouhlicky, D., Dones, L., et al. 2017, ApJ, 845, 27
Opitom, C., Yang, B., Selman, F., et al. 2019, A&A, 628, A128
Paganini, L., Blake, G. A., Villanueva, G. L., et al. 2013, IAUC, 9263, 3
Pajola, M., Höfner, S., Vincent, J. B., et al. 2017, European Planetary Science Congress, EPSC2017
Radeva, Y. L., Mumma, M. J., Bonev, B. P., et al. 2010, Icar, 206, 764
Radeva, Y. L., Mumma, M. J., Villanueva, G. L., et al. 2013, Icar, 2013, 298
Rayner, J., Bond, T., Bonnet, M., et al. 2012, Proc SPIE, 8446, 84462C
Rayner, J., Tokunaga, A., Jaffe, D., et al. 2016, Proc SPIE, 9908, 990884
Rickman, H., Marchi, S., A'Hearn, M. F., et al. 2015, A&A, 583, A44
Roth, N. X., Gibb, E. L., Bonev, B. P., et al. 2017, AJ, 153, 168
Roth, N. X., Gibb, E. L., Bonev, B. P., et al. 2018, AJ, 156, 251
Roth, N. X., Gibb, E. L., Bonev, B. P., et al. 2020, AJ, 159, 42
Roth, N. X., Milam, S. N., Cordiner, M. A., et al. 2021, ApJ, in press
Saki, M., Gibb, E. L., Bonev, B. P., et al. 2020a, AJ, 160, 184
Saki, M., Gibb, E. L., Bonev, B. P., et al. 2020b, BAAS, 52, 212.04

Sekanina, Z. 2010, ICQ, 32, 3
Sekanina, Z. 2014, arXiv:1409.7641
Sekanina, Z. 2017, arXiv:1712.03197
Sekanina, Z., Jehin, E., Boehnhardt, H., et al. 2002, ApJ, 572, 679
Shinnaka, Y., Ootsubo, T., Kawakita, H., et al. 2018, AJ, 156, 242
Stern, S. A. 2003, Natur, 424, 639
Tubbiolo, A. F., Gibson, B., Goggia, T., et al. 2015, MPEC, 2015, 1
Villanueva, G. L., DiSanti, M. A., Mumma, M. J., et al. 2012a, ApJ, 747, 3
Villanueva, G. L., Magee-Sauer, K., & Mumma, M. J. 2013, JQSRT, 129, 158
Villanueva, G. L., Mumma, M. J., Bonev, B. P., et al. 2009, ApJ, 690, L5
Villanueva, G. L., Mumma, M. J., Bonev, B. P., et al. 2012b, JQSRT, 113, 202
Villanueva, G. L., Mumma, M. J., DiSanti, M. A., et al. 2011a, Icar, 216, 227
Villanueva, G. L., Mumma, M. J., & Magee-Sauer, K. 2011b, JGR, 116, E08012
Villanueva, G. L., Mumma, M. J., Novak, R. E., & Hewagama, T. 2008, Icar, 195, 34
Villanueva, G. L., Smith, M. D., Protopapa, S., Faggi, S., & Mandell, A. M. 2018, JQSRT, 217, 86
Vincent, J. B., A'Hearn, M. F., Lin, Z. Y., et al. 2016, mnras, 462, S184
Vokrouhlický, D., Nesvorny`, D., & Dones, L. 2019, AJ, 157, 81
Wesołowski, M., Gronkowski, P., & Tralle, I. 2020, P&SS, 184, 104867
Wierzchos, K., & Womack, M. 2020, AJ, 159, 136
Yang, B., Hutsemékers, D., Shinnaka, Y., et al. 2018, A&A, 609, L4
Zolensky, M. E., Zega, T. J., Yano, H., et al. 2006, Sci, 314, 1735